CrystEngComm

ROYAL SOCIETY OF CHEMISTRY

COMMUNICATION

View Article Online
View Journal | View Issue

Cite this: *CrystEngComm*, 2025, **27**, 4258

Received 19th April 2025,
Accepted 29th May 2025

DOI: 10.1039/d5ce00425j

rsc.li/crystengcomm

Crystal growth of α-$AgSbS_2$ and its preliminary characterization for radiation detector applications†

Venika Ekanayake,[a] Matthew F. Webster,[b] Manipaul Dhillon,[c] David A. Kunar,[a] Serge Nagorny,[de] Mert Turfanda,[a] Michael P. Lewis[a] and Peng Li Wang *[ab]

α-$AgSbS_2$ materials have shown excellent photosensitivity in early studies, but the crystal growth and electrical properties were not reported. In this paper, we report the single crystal growth of α-$AgSbS_2$, its photoresponse characterization, and alpha particle radiation detection capability.

Room temperature radiation detector materials require specific physical and electrical properties to offer the best performance as radiation detectors.[1–5] These requirements include a high atomic number ($Z > 40$) to facilitate effective interaction with incoming radiation, and a wide band gap (1.5 eV $< E_g <$ 3 eV) to minimize leakage current and manage thermally generated electrons. Additionally, a close packed crystal structure is essential to optimize material density.[6] More importantly, a higher charge carrier mobility–lifetime product is crucial to achieve better charge collection efficiency and energy resolution of the detector. The mobility–lifetime product of a material is contingent upon its purity and the concentration of crystal defects in the semiconductor.[7,8] As a result, semiconducting radiation detectors are generally developed based on single crystalline materials.[2,3]

Due to these strict requirements, only a few semiconducting materials were successfully developed as room temperature radiation detectors, where cadmium zinc telluride is considered as the industry benchmark material. Nevertheless, cadmium zinc telluride still suffers from its compositional variations,[9] toxic heavy metal components, and difficult crystal synthesis and growth, which limit crystal size and induce high manufacturing costs, which hinder the material's commercialization. Furthermore, Si and high purity Ge semiconductor detectors are limited due to their low band gap values leading to high leakage current from thermally generated charge carriers. Therefore, Si and high-purity Ge detectors should be cryogenically cooled to maintain a better performance and cannot be used at room temperature.[10] Therefore, it is necessary to investigate and develop alternative semiconductor materials for room temperature radiation detector applications.

Ternary metal chalcogenide semiconductors are a class of materials composed of two different metals or metalloids and a chalcogen (S, Se, Te). They offer tunable band gaps and diverse stoichiometries with complex crystal structures, making them promising candidates for radiation detection due to their excellent physical and optoelectronic properties.[11,12]

Some ternary heavy metal chalcogenide semiconductors such as $Pb_2P_2Se_6$ and $Cs_2Hg_6S_7$ are known for their high densities (>6.0 g cm^{-3}) and acceptable resistivities (>10^6 Ω cm) at standard room temperature conditions.[7,13,14] Further, $Pb_2P_2Se_6$ exhibits high Knoop hardness (106 kg mm^{-2}), which plays a crucial role in crystal processing, as softer materials may undergo stresses and damage during cutting, polishing and handling.[15] Thus, hardness is a key factor in both detector materials and fabrication processes. However, many ternary heavy metal chalcogenide semiconductor materials contain toxic heavy metal elements to achieve a high effective atomic mass and density.

Ag–Sb–S-based ternary metal chalcogenide semiconductors have been highlighted for their non-toxicity, excellent optoelectrical properties, high density, and superior hardness, making them viable candidates for radiation detectors. The phase diagram of ternary Ag–Sb–S reveals three distinct phases: Ag_5SbS_4, $AgSbS_2$ and Ag_3SbS_3.[16] Among these, $AgSbS_2$ shows outstanding optical absorption, spanning the entire visible to infrared range, with a high absorption coefficient of $\alpha = 10^5$ cm^{-1}.[17–20]

$AgSbS_2$ exhibits two polymorphs: a low-temperature monoclinic form (α-$AgSbS_2$, miargyrite) and a high-temperature

[a] *Department of Chemistry, Queen's University, Kingston, Ontario, Canada. E-mail: wang.peng@queensu.ca*
[b] *Department of Physics, Engineering Physics & Astronomy, Queen's University, Kingston, Ontario, Canada*
[c] *Department of Chemistry, University of British Columbia, Vancouver, BC, Canada*
[d] *Gran Sasso Science Institute, L'Aquila, I-67100, AQ, Italy*
[e] *INFN – Laboratori Nazionali del Gran Sasso, Assergi, I-67100, AQ, Italy*

† Electronic supplementary information (ESI) available. See DOI: https://doi.org/10.1039/d5ce00425j

cubic form (β-$AgSbS_2$, cuboargyrite).[21] The monoclinic form undergoes inversion to the cubic phase at 380 °C, representing a presumed first-order phase transition.[22]

Previous studies on polycrystalline $AgSbS_2$ primarily focused on thin films using precursor methods such as spin coating, evaporation, sputtering, and two-stage processes like sulfurizing thermally evaporated Sb/Ag. These thin films were investigated for use as photodetectors, photovoltaic devices, rewritable optical data recording devices, and photochemical water splitting applications.[17,23–25] Additionally, $AgSbS_2$ nanomaterials were synthesized through wet chemistry and solvothermal methods for potential use as a solar absorber material and an anode material for Li-ion batteries.[26,27]

However, all of the above mentioned studies focused on the growth of $AgSbS_2$ in the form of thin films, which are not suitable for radiation detection due to the presence of numerous grain boundaries that limit charge transport and reduce detector performance. To the best of our knowledge, no previous studies have reported the growth of bulk single crystalline $AgSbS_2$ compounds to be used as room temperature radiation detectors. In the present study, we address this gap by growing bulk $AgSbS_2$ single crystals with large boundaries and defect free volume using the vertical Bridgman method, which results in photosensitive devices with a higher signal-to-noise ratio compared to previous studies.

In this study, we present a comprehensive investigation of the purification of elemental precursors, synthesis, and single crystal growth of $AgSbS_2$ through a modified vertical Bridgman method (all details in chronological order are presented in the ESI† document). Furthermore, we have conducted a thorough examination of the material's physical properties, an assessment of its electrical properties, and an evaluation of its photoelectrical behaviour under visible light, as well as under irradiation by alpha particles.

$AgSbS_2$ crystals (Fig. 1(a)) were grown by the vertical Bridgman method as explained in Fig. S2† by following the temperature profile shown in Fig. S3.† To verify the existence of the two phases of $AgSbS_2$, a heated $AgSbS_2$ sample at 480 °C was rapidly quenched in cold water and compared against the $AgSbS_2$ sample that followed the complete growth process. The pXRD pattern of the quenched sample (Fig. 1(c), green pattern) confirms the presence of the β-$AgSbS_2$ phase adopting the space group $Fm\bar{3}m$.

The pXRD pattern of the Bridgman-grown $AgSbS_2$ crystal displays distinct characteristic peaks from the monoclinic α-$AgSbS_2$ phase adopting the $C2/c$ space group, which is consistent with reported data (Fig. 1(c), purple pattern).[28] This also confirms that the α-$AgSbS_2$ phase transforms into the β-$AgSbS_2$ phase at temperatures above 380 °C. Additionally, no diffraction peaks corresponding to the Ag_2S, Sb_2S_3, or cubic β-$AgSbS_2$ phases were observed, confirming high phase purity of the grown crystal.

The XRD pattern of the crystal wafer (Fig. 1(b)), cut perpendicular to the growth direction, is shown in Fig. 1(c), lowest pattern. Peaks at 43.255° and 63.534° originate from the steel sample holder. The prominent peak at 32.569° corresponds to the (204) crystal lattice plane (Fig. 1(c), red pattern). This confirms that monoclinic α-$AgSbS_2$ was grown with high crystallinity along a single axis normal to the (204) lattice plane without any twinning occurring within the crystal. The full width at half maximum (FWHM) of the (204) peak is (0.2721 ± 0.0025)°, which also

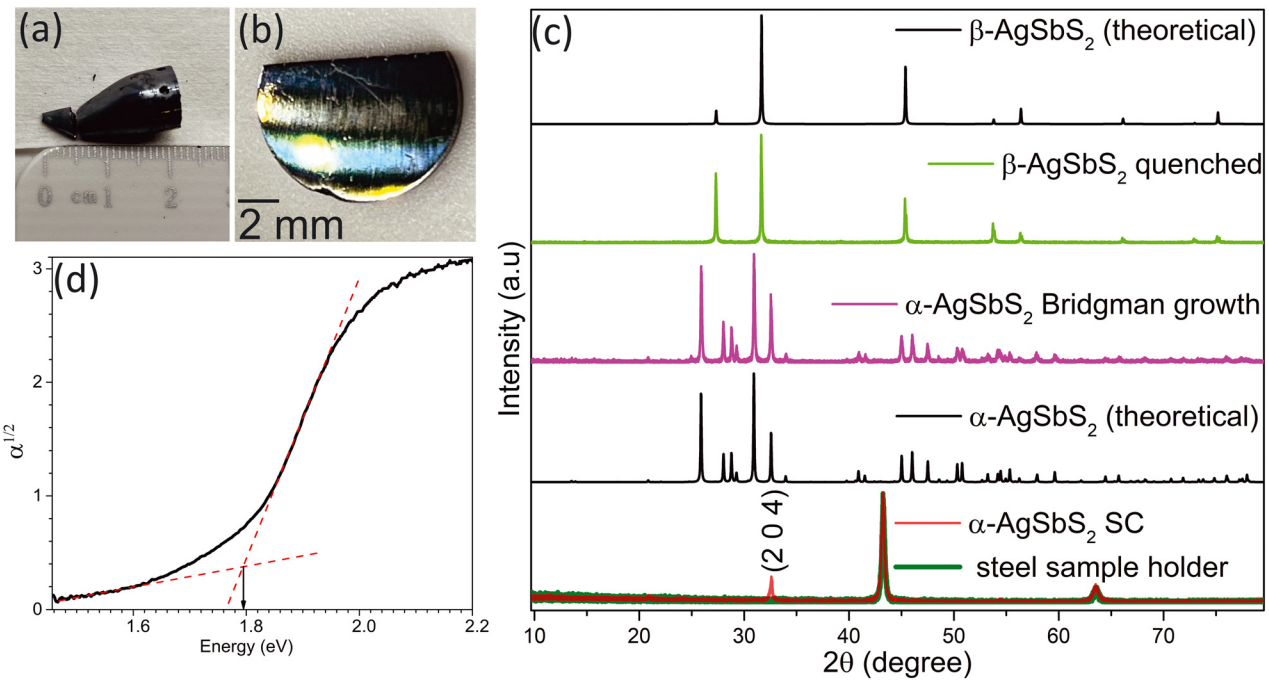

Fig. 1 (a) The as-grown $AgSbS_2$ ingot produced by vertical Bridgman technique, (b) polished $AgSbS_2$ crystal wafer, (c) powder X-ray diffraction patterns of the cubic (β-$AgSbS_2$) and monoclinic (α-$AgSbS_2$) phases, and the X-ray diffraction pattern of the single crystal, and (d) Tauc plot.

confirms lower mosaicity leading to a higher degree of order and uniformity within the crystal.[29]

Higher degree of crystallinity of α-$AgSbS_2$ offers significant advantages over the polycrystalline forms due to the absence of grain boundaries and associated defects. In polycrystalline $AgSbS_2$, grain boundaries act as recombination sites for trapped charge carriers, reducing the carrier mobility and creating potential barriers that hinder charge transport.[30,31] These barriers lead to media polarization and reduce the charge collection efficiency when the detector operates under an applied bias.[32] Additionally, charge accumulation at grain boundaries can distort the internal electric field, further diminishing the effectiveness of the applied external bias and limiting the charge collection at the contacts.

The microindentation measurements revealed that $AgSbS_2$ possesses a Knoop hardness of 121 ± 10 kg mm^{-2} (Fig. S7, Table S1 in ESI†). The measured hardness of $AgSbS_2$ exceeds that of other chalcogenides, such as $Cd_{1-x}Zn_xTe$ (60–80 kg mm^{-2})[33] and $Pb_2P_2Se_6$ (106 ± 3 kg mm^{-2}),[15] indicating that $AgSbS_2$ is notably harder than these materials. This superior hardness contributes to the mechanical resilience of $AgSbS_2$ crystals, making them well-suited for conventional semiconductor processing and device fabrication procedures.

According to the Tauc plot shown in Fig. 1(d), the $AgSbS_2$ band gap was determined to be 1.79 eV, thereby aligning within the reported band gap range of 1.73–1.83 eV.[17,25] According to previous studies on $AgSbS_2$'s band structure and density of states, the valence band and conduction band are primarily dominated by the S 3p states, with hybridization from the Sb 5p states and minimal contribution from the Ag 4d states. This suggests that sulfur plays a crucial role in determining the bandgap of the material.[34]

Photosensitive devices were fabricated by polishing crystals of α-$AgSbS_2$ as shown in Fig. 1(b). Current–voltage (*I–V*) characteristics of the Ag/$AgSbS_2$/Ag device configuration were evaluated through a bias range of 100–700 V as shown in Fig. S8.† Notably, this device exhibits ohmic behaviour through the voltage range signifying a minimal charge accumulation and showing a tolerance to higher applied potentials. As can be concluded from the linear *I–V* curves, the resistivity of the crystalline α-$AgSbS_2$ is 2.4 × 10^9–3.7 × 10^{10} Ω cm, which is in the range of the resistivity of cadmium zinc telluride crystals.[35] Higher resistivity of the material will reduce the dark current, thus improving the signal-to-noise ratio and enabling the device to detect radiation with a lower energy threshold. Also, the low dark current allows the detector to produce a signal at room temperature without the need to be cooled.[36]

To study the device performance with different contacting systems, Au and In were deposited onto the surface of the crystal by e-beam evaporation to obtain the AuIn/$AgSbS_2$/Au device configuration as shown in Fig. 2(a). *I–V* characteristics and photoresponse behaviour were compared with the Ag/$AgSbS_2$/Ag device (Fig. 2(b)) across an applied bias range (from 100 to 200 V). The Ag/$AgSbS_2$/Ag devices show less resistive ohmic behaviour compared to the AuIn/$AgSbS_2$/Au device.

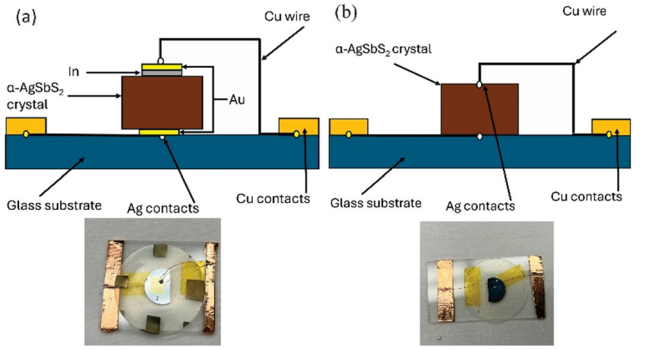

Fig. 2 Schematicdiagram of fabricated devices: (a) AuIn/$AgSbS_2$/Au and (b) Ag/$AgSbS_2$/Ag.

The change in conductive behaviour happens when there is a certain mismatch of the work function between the silver metal and $AgSbS_2$, creating a different type of resistive ohmic contact, while the indium–$AgSbS_2$ interface tends to be more conductive by bringing the barrier height near zero, making it a better ohmic contact.[37] This also determines that α-$AgSbS_2$ may have a work function closer to indium metal which is 4.09 eV.[38]

Moreover, linearity in the *I–V* behaviour of these two devices could be due to the field emission tunnelling conducting mode.[39] Furthermore, negligible resistance of the contact compared to the resistance of the bulk semiconductor material and linear *I–V* curves reveals that the Ag/$AgSbS_2$/Ag device has an unimpeded transfer of charge carriers to its contacts and does not affect or modify the detector signal compared to the AuIn/$AgSbS_2$/Au device configuration.[40]

To study the time-dependent photoresponse of the Ag/$AgSbS_2$/Ag device, it was irradiated with a white LED at an optical power of 24 mW over multiple cycles of illumination, alternating light-on and light-off for 10-second-long time intervals. The Ag/$AgSbS_2$/Ag device was biased under different constant voltages ranging from 100–700 V (Fig. S9†). Ag/$AgSbS_2$/Ag devices have shown a considerable increase in the photocurrents compared to the dark current under light illumination with a signal-to-noise ratio of 1.7, which does not depend on the external bias potential. The curves showed a rapid and reproducible photocurrent response with excellent cycling stability, where the photogenerated current increased immediately under illumination and returned to its original value when the light was turned off. During illumination, light photons are absorbed by the $AgSbS_2$ crystal generating electron–hole pairs. These charge carriers drift to the contacts due to the applied bias and generate the photocurrent.

By using the same setup, we have tested the photocurrent response of AuIn/$AgSbS_2$/Au devices as shown in Fig. 3(b) across the 100 to 200 V bias range exhibiting a signal-to-noise ratio of 1.4.

An increase in the baseline current with higher bias potential, as seen in Fig. 3(b), is likely due to bulk leakage currents arising from thermally generated carriers and

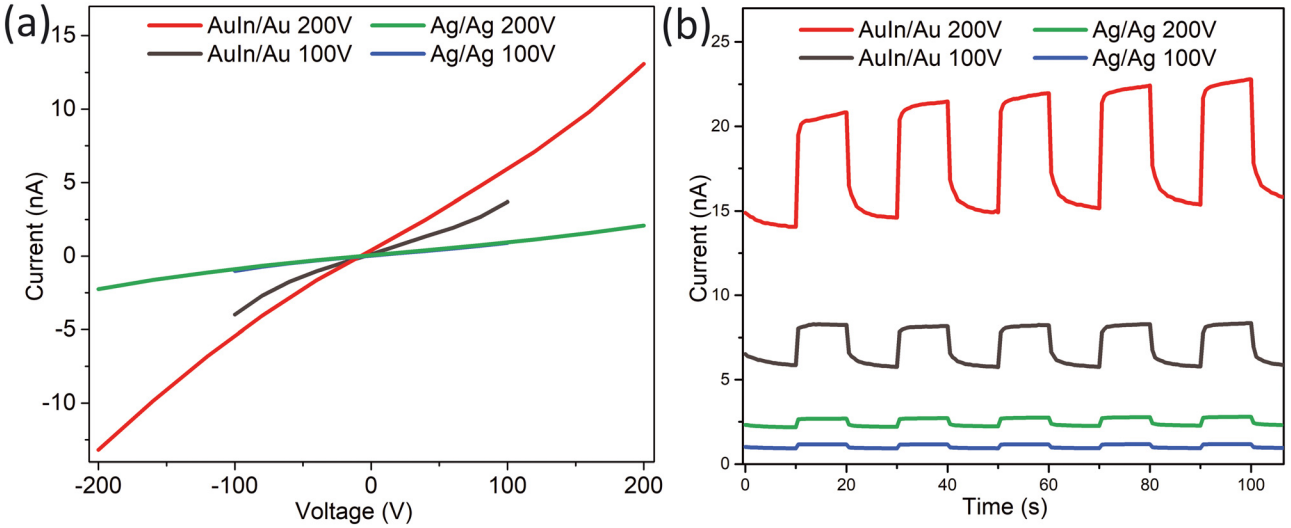

Fig. 3 Electrical measurements of Ag/$AgSbS_2$/Ag and AuIn/$AgSbS_2$/Au device configurations. (a) *I–V* characteristics and (b) photoresponse of devices illuminated under 24 mW white LED.

crystal imperfections.[41] It was also observed that the dark current was increased compared to the Ag/Ag contacts, while the photocurrent responses were sharp upon activating the LED with a slow decay time when the light was turned off indicating a slower charge-detrapping process in the material.

To compare the time profile of the photoresponse pulse for two device types, the response time (τ) was considered as shown in Fig. 4(a) and (b). The response time is comprised of the rise time (τ_{rise}), denoting the duration for the net photocurrent to elevate from 10% to 90% of its saturation value, and the decay time (τ_{decay}), indicating the duration for the net photocurrent to decrease from 90% to 10% of its saturation value.[20,42] In Fig. 4(a), for the AuIn/$AgSbS_2$/Au detector, τ_{rise}/τ_{decay} = 875/3100 ms. In contrast, as shown in Fig. 4(b), the Ag/$AgSbS_2$/Ag detector exhibits a τ_{rise}/τ_{decay} = 425/3470 ms. In both devices, it is observed that $\tau_{rise} < \tau_{decay}$, indicating delayed extraction of photogenerated carriers due to trapping within the crystal.[43] The response time of Ag/$AgSbS_2$/Ag detectors is around 1.5 orders of magnitude lower than previous photodetectors produced by $AgSbS_2$ alone, while the decay time of photoresponse pulse is 35 times shorter.[20] This could be due to low concentration of defects and shallow traps in the crystalline detector compared to the polycrystalline photodetectors fabricated by spin-coating. Even though the τ_{decay} for AuIn/$AgSbS_2$/Au devices is shorter than those for the Ag/$AgSbS_2$/Ag devices, we can determine that the Ag/$AgSbS_2$/Ag devices have better sensitivity as a photodetector, since τ_{rise} is shorter.

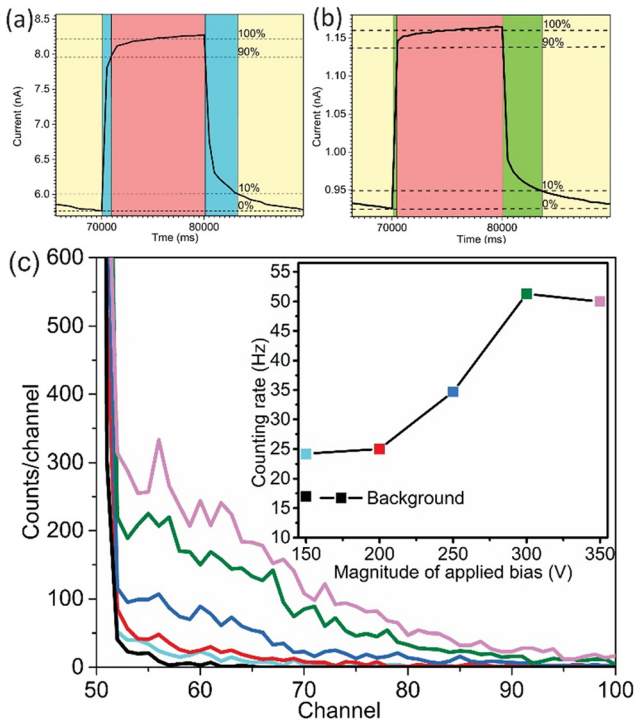

Fig. 4 Time-profile of the photoresponse pulse of (a) AuIn/$AgSbS_2$/Au and (b) Ag/$AgSbS_2$/Ag devices measured at 100 V of bias, and (c) pulse-height spectra of $AgSbS_2$ with the ^{241}Am alpha source; the inset is the counting rate *vs.* applied bias (colours online).

The Ag/$AgSbS_2$/Ag device underwent pulse-height measurement (Fig. 4(c)) by exposure to an ^{241}Am alpha particle source with an activity of 0.9 μCi under a negative applied bias to collect holes. Background data collection was conducted over the same time interval without any radiation source at −150 V bias potential. In comparison to the background data, a distinct response was observed in the charge collected under irradiation by the ^{241}Am source at −150 V bias potential. As the magnitude of the bias potential across the sample increased from −150 to −350 V, a higher counting rate was recorded, providing additional confirmation of the sample's responsiveness to the radiation source. As shown in the inset of Fig. 4(c), the charge collection efficiency increases with the applied bias up to 300 V, as indicated by the rising counting rate. A slight decrease

in the counting rate between 300 and 350 V may be attributed to reduced charge collection efficiency, possibly due to bulk polarization. The spectroscopic features of the ^{241}Am alpha particle radiation were not resolved. It is plausible that the presence of electronic defects related to intrinsic impurities may have limited the device's performance as a radiation detector. Addressing these issues requires continuous refinement in crystal growth and fabrication techniques.

In summary, α-$AgSbS_2$ single crystals were grown using the vertical Bridgman method, confirming high phase purity of monoclinic α-$AgSbS_2$ by p-XRD. The material exhibited high crystallinity, higher hardness (121 ± 10 kg mm^{-2}) than cadmium zinc telluride and other chalcogenides, and a band gap of 1.79 eV. Ag/$AgSbS_2$/Ag devices demonstrated high resistivity (2.4×10^9–3.7×10^{10} Ω cm), low dark current in the nanoampere range, and higher sensitivity to light photons. Pulse-height measurements confirmed α-radiation response. In the future, improved fabrication and growth techniques are essential to enhance detector performance by minimizing electronic defects.

Data availability

Additional data supporting this article have been included as a part of ESI.† Data for this article, including UV-Vis, XRD, electrical measurements and alpha response data are available at Queen's University Dataverse Collection at **https://doi.org/10.5683/SP3/H97YRL**.

Author contributions

V. E., M. D. and D. A. K.: investigation, visualization, and writing – original draft. P. L. W. and V. E.: conceptualization, methodology, and validation. V. E., M. P. L. and M. T.: characterization and data analysis. M. F. W. and V. E.: data curation. P. L. W. and S. N.: project administration, supervision, writing – review & editing. M. F. W.: software.

Conflicts of interest

There are no conflicts to declare.

Notes and references

1 M. Schieber, *Nucl. Instrum. Methods*, 1977, **144**, 469–477.
2 J. Androulakis, S. C. Peter, H. Li, C. D. Malliakas, J. A. Peters, Z. Liu, B. W. Wessels, J. H. Song, H. Jin, A. J. Freeman and M. G. Kanatzidis, *Adv. Mater.*, 2011, **23**, 4163–4167.
3 T. E. Schlesinger, J. E. Toney, H. Yoon, E. Y. Lee, B. A. Brunett, L. Franks and R. B. James, *Mater. Sci. Eng., R*, 2001, **32**, 103–189.
4 D. A. Kunar, M. F. Webster, Y. Wu, R. Kandel and P. L. Wang, *Crystals*, 2023, **13**, 762.
5 K. Hitomi, T. Tada, S. Kim, Y. Wu, T. Tanaka, T. Shoji, H. Yamazaki and K. Ishii, *IEEE Trans. Nucl. Sci.*, 2011, **58**, 1987–1991.
6 A. Mirzaei, J.-S. Huh, S. S. Kim and H. W. Kim, *Electron. Mater. Lett.*, 2018, **14**, 261–287.
7 P. L. Wang, S. S. Kostina, F. Meng, O. Y. Kontsevoi, Z. Liu, P. Chen, J. A. Peters, M. Hanson, Y. He, D. Y. Chung, A. J. Freeman, B. W. Wessels and M. G. Kanatzidis, *Cryst. Growth Des.*, 2016, **16**, 5100–5109.
8 R. Kandel, M. F. Webster, A. Hart, R. Poushimin, A. Nikniazi, J. M. Nunzi, M. Bazalova-Carter and P. L. Wang, *ACS Appl. Mater. Interfaces*, 2021, **13**, 56296–56301.
9 J. E. Toney, B. A. Brunett, T. E. Schlesinger, J. M. Van Scyoc, R. B. James, M. Schieber, M. Goorsky, H. Yoon, E. Eissler and C. Johnson, *Nucl. Instrum. Methods Phys. Res., Sect. A*, 1996, **380**, 132–135.
10 D. Pennicard, B. Pirard, O. Tolbanov and K. Iniewski, *MRS Bull.*, 2017, **42**, 445–450.
11 S. Johnsen, Z. Liu, J. A. Peters, J.-H. Song, S. C. Peter, C. D. Malliakas, N. K. Cho, H. Jin, A. J. Freeman, B. W. Wessels and M. G. Kanatzidis, *Chem. Mater.*, 2011, **23**, 3120–3128.
12 M. Bouroushian, *Electrochemistry of Metal Chalcogenides*, Springer Berlin Heidelberg, Berlin, Heidelberg, 2010.
13 V. Ekanayake, A. Hart, R. Kandel, S. Nagorny, K. McEleney, M. Bazalova and P. L. Wang, *IEEE Trans. Nucl. Sci.*, 2025, 1.
14 H. Li, J. A. Peters, Z. Liu, M. Sebastian, C. D. Malliakas, J. Androulakis, L. Zhao, I. Chung, S. L. Nguyen, S. Johnsen, B. W. Wessels and M. G. Kanatzidis, *Cryst. Growth Des.*, 2012, **12**, 3250–3256.
15 P. L. Wang, Z. Liu, P. Chen, J. A. Peters, G. Tan, J. Im, W. Lin, A. J. Freeman, B. W. Wessels and M. G. Kanatzidis, *Adv. Funct. Mater.*, 2015, **25**, 4874–4881.
16 R. Schmid Fetzer, in *Ternary alloys: a comprehensive compendium of evaluated constitutional data and phase diagrams*, ed. G. Petzow and G. Effenberg, VCH, Weinheim, Federal Republic of Germany, 1988, vol. 2, pp. 512–520.
17 Y. Yang, H. Huang, S. Bai, F. Yao and Q. Lin, *J. Phys. Chem. Lett.*, 2022, 8086–8090.
18 A. Nadukkandy, S. Devasia, P. Abraham, S. Shaji, D. A. Avellaneda, J. A. Aguilar-Martínez, E. G. Martinez, R. F. Cienfuegos-Pelaes and B. Krishnan, *Mater. Sci. Semicond. Process.*, 2021, **135**, 106074.
19 S. Bai, R. Li, Y. Yang, Z. Jia, B. Yu, Y. Liu, F. Yao, H. Huang and Q. Lin, *Adv. Phys. Res.*, 2023, **2**(6), 2200111.
20 W. Zhai, W. Zheng, Z. Zhang, L. Huang, B. Yu, L. Chen, G. Li, X. Li, X. Zhou, L. Lin, Z. Yan, C. Chen, X. Jiang and J.-M. Liu, *J. Phys. Chem. C*, 2023, **127**, 18778–18783.
21 I. Y. Nekrasov and S. E. Lunin, *Mineral. Mag.*, 1987, **9**, 25–28.
22 A. Orliukas, V. Valiukenas, V. Kybartas and A. Kezionis, *Ferroelectrics*, 1981, **38**, 897–900.
23 T. Daniel, J. Henry, K. Mohanraj and G. Sivakumar, *Mater. Chem. Phys.*, 2016, **181**, 415–421.
24 J. Gutwirth, T. Wagner, M. Vlcek, C. Drasar, L. Benes, M. Hrdlicka, M. Frumar, J. Schwarz and H. Ticha, *MRS Online Proc. Libr.*, 2006, **918**, 7010801.

25 U. Chalapathi, Y. B. K. Kumar, A. Sreedhar, V. Gonuguntla, N. H. Alotaibi, P. Rosaiah and S.-H. Park, *J. Solid State Chem.*, 2024, **334**, 124691.
26 E. Saksornchai, J. Kavinchan, S. Thongtem and T. Thongtem, *Chalcogenide Lett.*, 2017, **14**, 483–488.
27 S.-F. Ho, Y.-C. Yang and H.-Y. Tuan, *J. Colloid Interface Sci.*, 2022, **621**, 416–430.
28 H. Effenberger, W. H. Paar, D. Topa, A. J. Criddle and M. Fleck, *Am. Mineral.*, 2002, **87**, 753–764.
29 M. S. Goorsky, H. Yoon, M. Schieber, R. B. James, D. S. McGregor and M. Natarajan, *Nucl. Instrum. Methods Phys. Res., Sect. A*, 1996, **380**, 6–9.
30 S. N. Mohammad and C. E. Rogers, *Solid-State Electron.*, 1988, **31**, 1157–1167.
31 A. E. Bolotnikov, G. S. Camarda, Y. Cui, G. Yang, A. Hossain, K. Kim and R. B. James, *J. Cryst. Growth*, 2013, **379**, 46–56.
32 H. L. Malm and M. Martini, *IEEE Trans. Nucl. Sci.*, 1974, **21**, 322–330.
33 S. Mcdevitt, D. R. John, J. L. Sepich, K. A. Bowers, J. F. Schetzina, R. S. Rai and S. Mahajan, *Proc. MRS.*, 1989, **161**, 15.
34 A. Benslimane, S. Kouidri, H. Rached, M. El Keurti, S. Meliani and M. Ould Moussa, *Indian J. Phys.*, 2024, **98**, 955–966.
35 A. A. Melnikov, A. S. Sigov, K. A. Vorotilov, A. A. Davydov, L. I. Topalova and N. V. Zhavoronkov, *J. Cryst. Growth*, 1999, **197**, 666–669.
36 J. Chen, H. Tang, Z. Li, Z. Zhu, M. Gu, J. Xu, X. Ouyang and B. Liu, *Opt. Express*, 2021, **29**, 23292.
37 E. Frau, D. Sam-Giao, A. Kerlain and C. Brylinski, *J. Electron. Mater.*, 2024, **53**, 8098–8107.
38 X. D. Hong, D. Liang and Q. Y. Zhang, *Phys. E*, 2024, **156**, 115841.
39 A. Piotrowska, A. Guivarc'h and G. Pelous, *Solid-State Electron.*, 1983, **26**, 179–197.
40 E. H. Rhoderick, *IEE Proc., Part I*, 1982, **129**, 1.
41 A. Owens, *Compound Semiconductor Radiation Detectors*, CRC Press, 2016.
42 H. Pi, X. Li, L. Xie, Y. Cui, L. Jing, B. Chen, Y. Wang and A. L. Rogach, *Adv. Opt. Mater.*, 2025, **13**(14), 2403489.
43 K. Domanski, W. Tress, T. Moehl, M. Saliba, M. K. Nazeeruddin and M. Grätzel, *Adv. Funct. Mater.*, 2015, **25**, 6936–6947.